Supporting Information

First-row transition-metal carbide nanosheets as high-performance cathode materials for lithium-sulfur batteries

Imran Muhammad[a,†], Shehzad Ahmed[b,†], Zhen Yao[a], Danish Khan[c], Tanveer Hussain[d], and Yang-Gang Wang[a]*

[a]Department of Chemistry and Guangdong Provincial Key Laboratory of Catalytic Chemistry, Southern University of Science and Technology, Shenzhen, Guangdong 518055, China.

[b]College of Physics and Optoelectronic Engineering, Shenzhen University, Guangdong 518060, China.

[c]College of New Materials and New Energies, Shenzhen Technology University, Shenzhen 518118, Guangdong, China.

[d]School of Science and Technology, University of New England, Armidale, New South Wales 2351, Australia.

Corresponding Author: Yang-Gang Wang (wangyg@sustech.edu.cn)

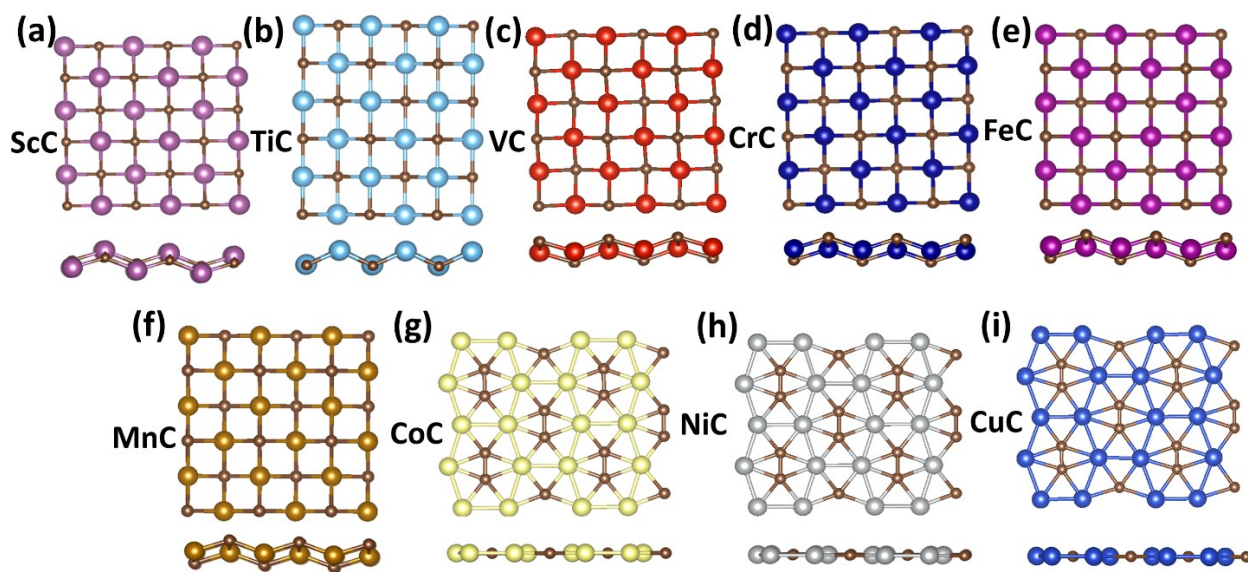Imran Muhammad and Shehzad Ahmed contributed equally as the first co-authors.

Figure S1. Relaxed geometric structures of (a) ScC, (b) TiC, (c) VC, (d) CrC, (e) MnC, (f) FeC in tetragonal and (g) CoC, (h) NiC, (i) CuC in the orthorhombic lattice.
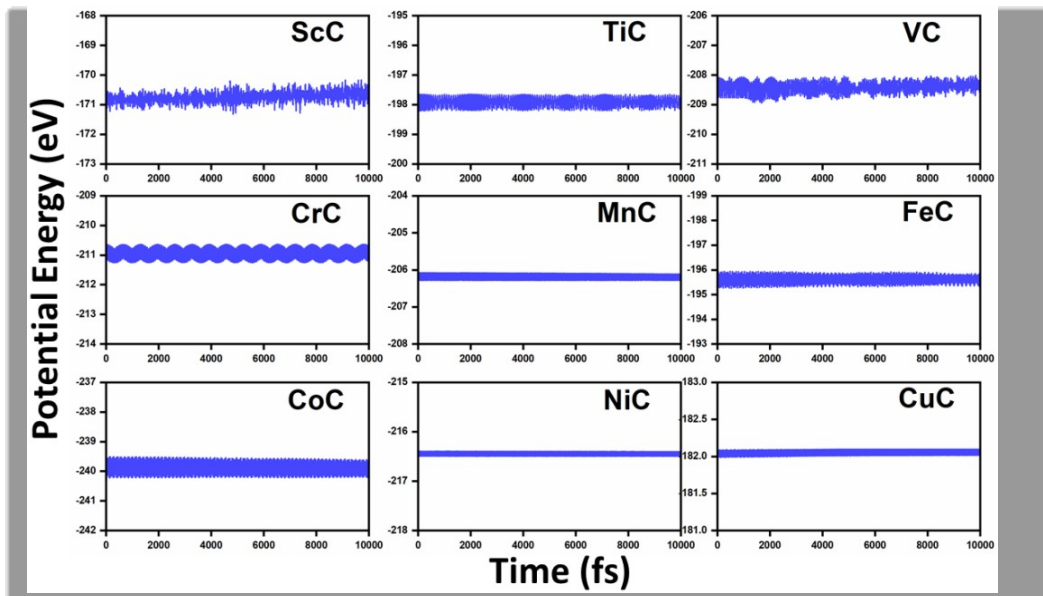
Figure S2. AIMD simulations for all TMC-based nanostructures during the time of 10 ps at a temperature of 300 K.
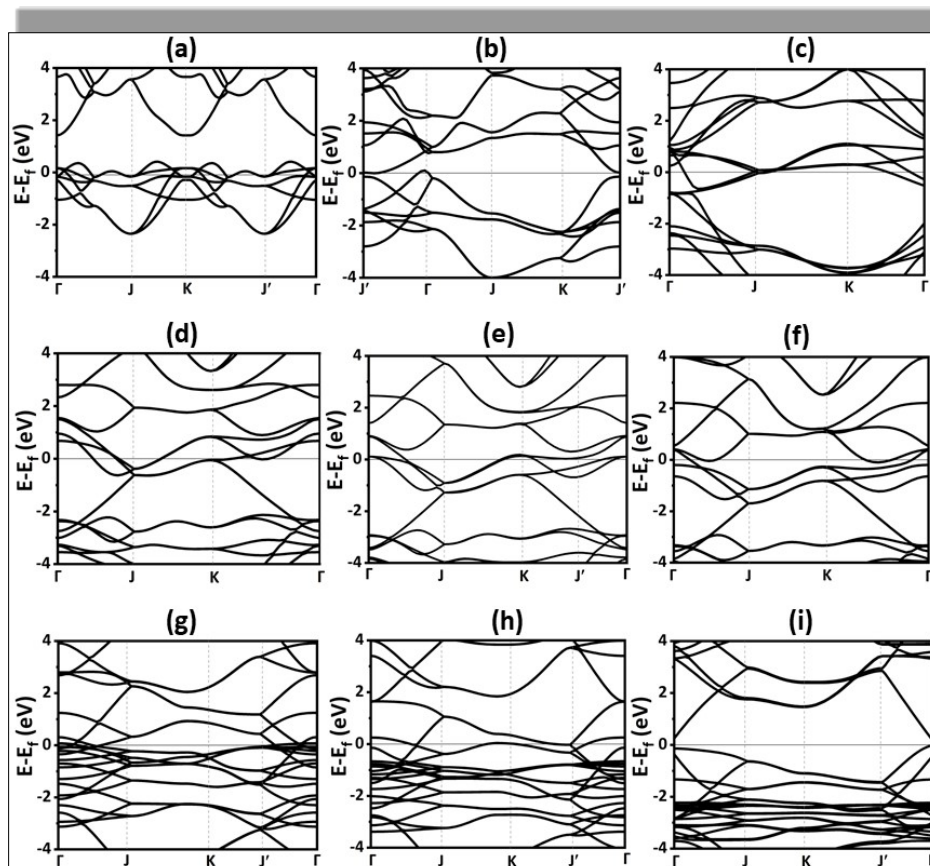

Figure S3. Electronic band structures of (a) ScC, (b) TiC, (c) VC (d) CrC, (e) MnC, (f) FeC, (g) CoC, (h) NiC, and CuC nanostructures.
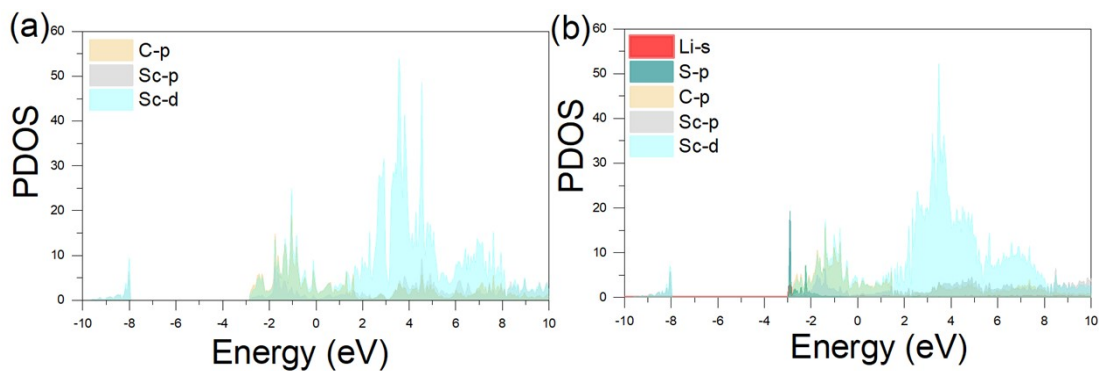
Figure S4. The orbital-projected densities of states for (a) pristine and (b) Li_2S cluster adsorbed ScC nanosheet at the PBE level where Fermi levels are set to zero.
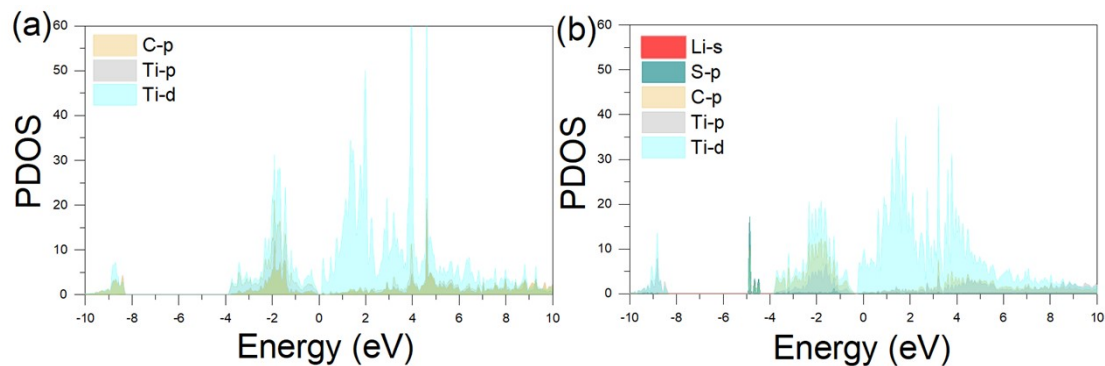

Figure S5. The orbital-projected densities of states for (a) pristine and (b) Li_2S cluster adsorbed TiC nanosheet at the PBE level where Fermi levels are set to zero.

Figure S6. The orbital-projected densities of states for (a) pristine and (b) Li_2S cluster adsorbed VC nanosheet at the PBE level where Fermi levels are set to zero.
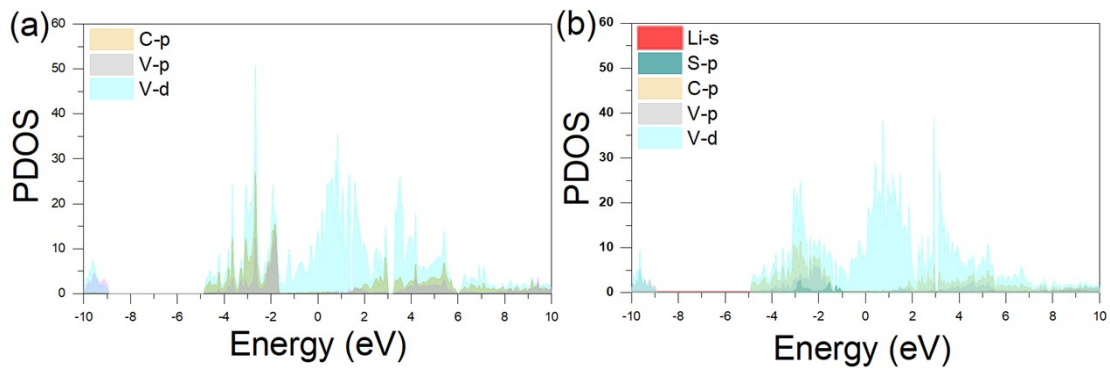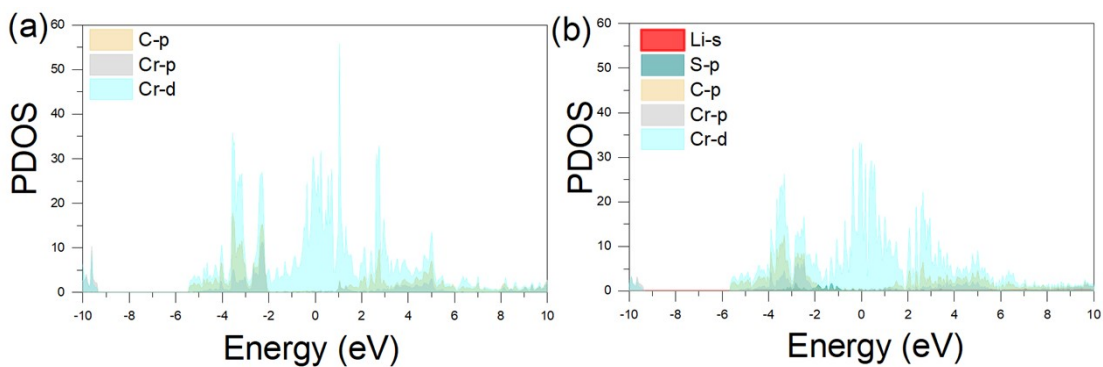
Figure S7. The orbital-projected densities of states for (a) pristine and (b) Li$_2$S cluster adsorbed CrC nanosheet at the PBE level where Fermi levels are set to zero.

Figure S8. The orbital-projected densities of states for (a) pristine and (b) Li$_2$S cluster adsorbed MnC nanosheet at the PBE level where Fermi levels are set to zero.
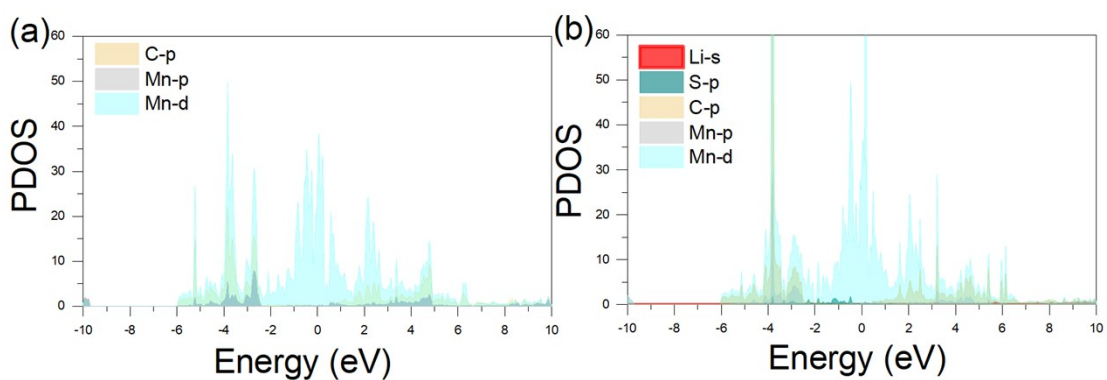

Figure S9. The orbital-projected densities of states for (a) pristine and (b) Li$_2$S cluster adsorbed FeC nanosheet at the PBE level where Fermi levels are set to zero.
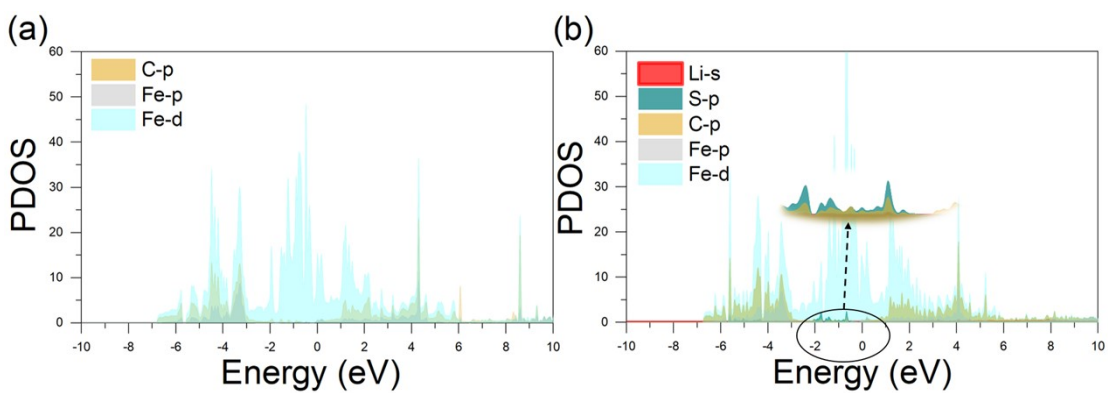
Figure S10. The orbital-projected densities of states for (a) pristine and (b) Li$_2$S cluster adsorbed CoC nanosheet at the PBE level where Fermi levels are set to zero.

Figure S11. The orbital-projected densities of states for (a) pristine and (b) Li$_2$S cluster adsorbed NiC nanosheet at the PBE level where Fermi levels are set to zero.

Figure S12. The orbital-projected densities of states for (a) pristine and (b) Li$_2$S cluster adsorbed CuC nanosheet at the PBE level where Fermi levels are set to zero.
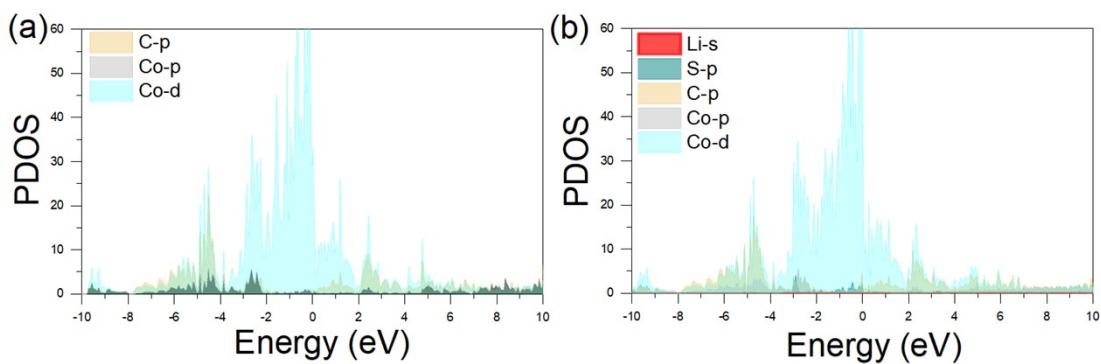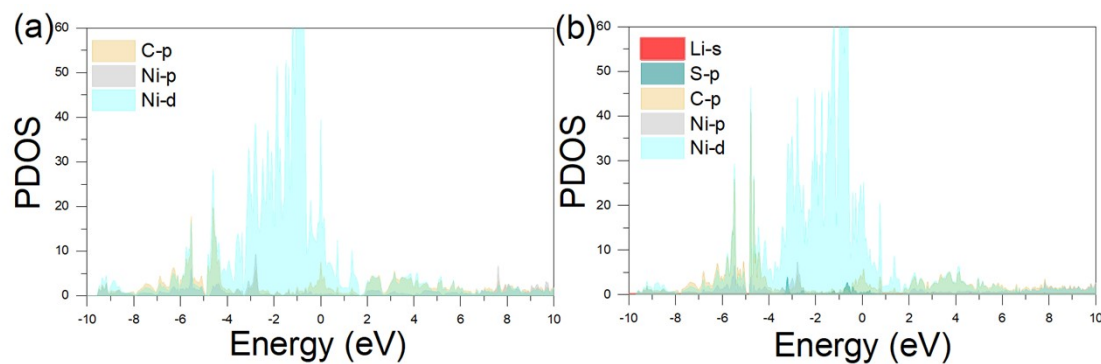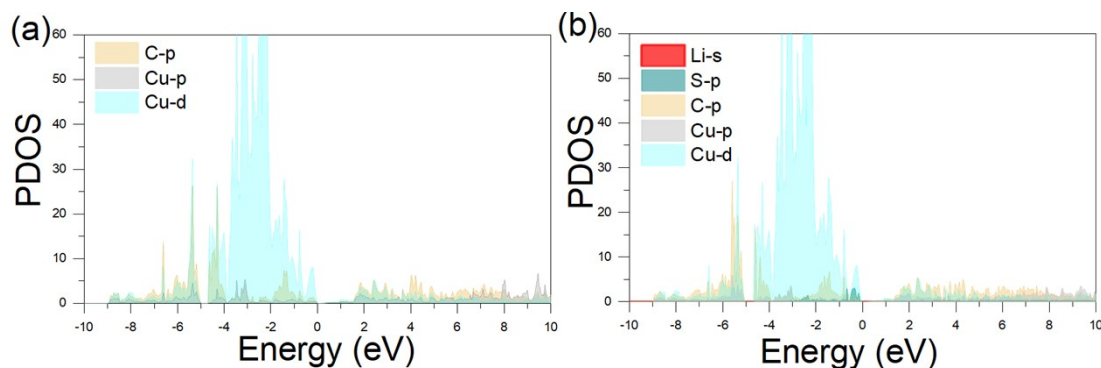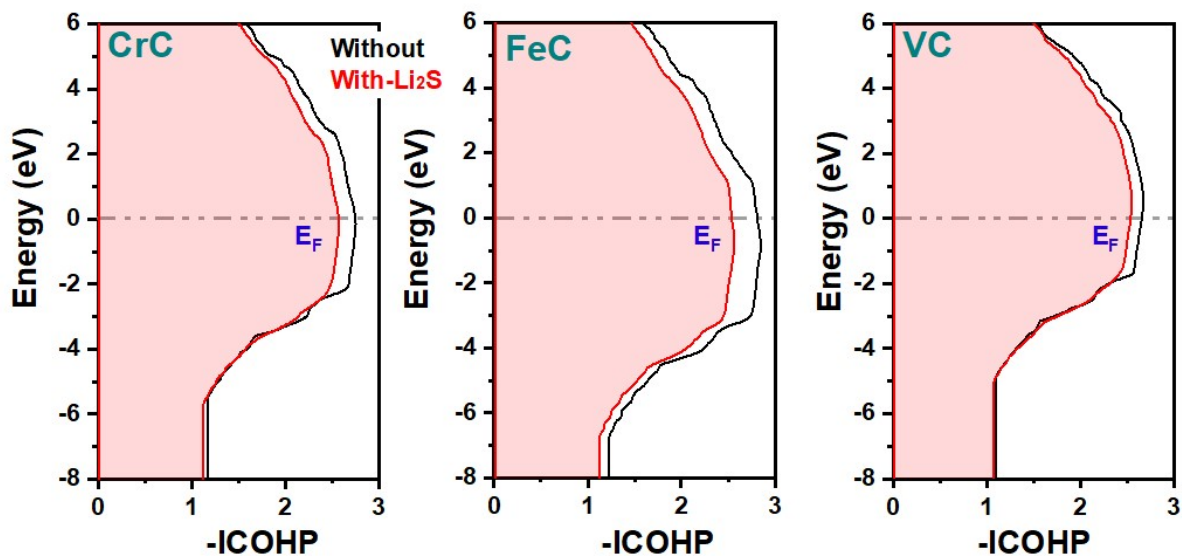
Figure S13. Integrated COHP (ICOHP) for pristine and Li$_2$S cluster adsorbed CrC, FeC, and VC nanosheets where Fermi levels are set to zero.
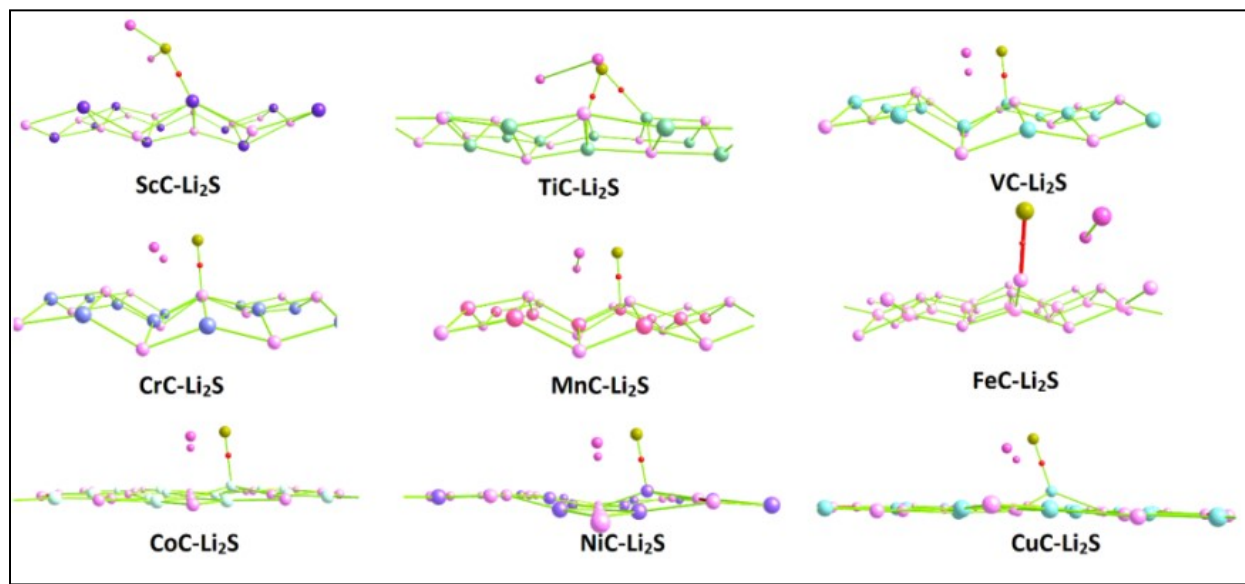

Figure S14. AIM plots for Li$_2$S adsorption onto TMCs. The bond critical point (BCP) is represented by a small red ball between the S atom and TMCs. In AIM plots, the interaction site's BCP is mentioned for clarity.

The variation in Gibbs free energy is calculated by employing the following equation:

$$\Delta G = \Delta E_{AD} - T\Delta S + \Delta ZPE \qquad (S1)$$

Where ΔE_{AD} shows the difference in energies before and after the sulfur reduction reaction, while $T\Delta S$ and ΔZPE present the changes in the entropy and zero-point energies respectively.
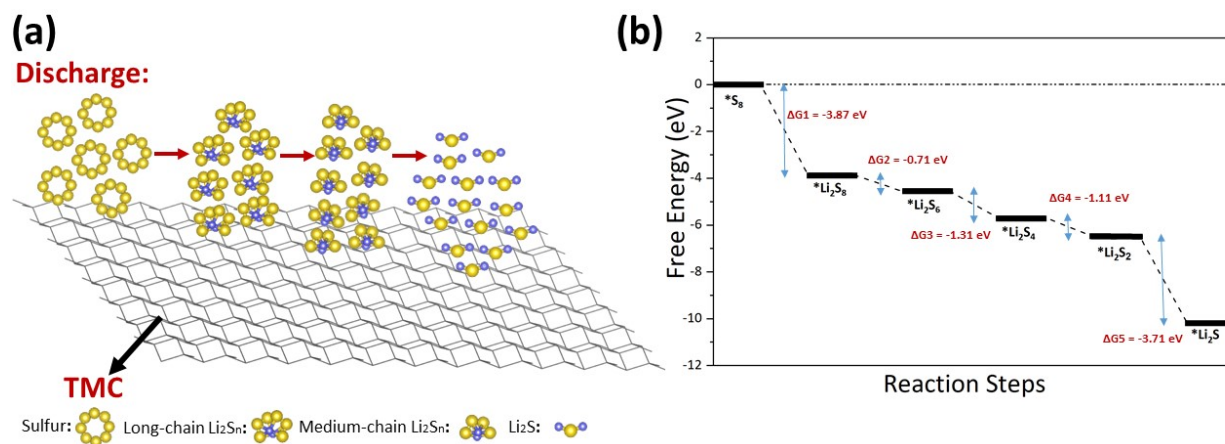
Figure S15. (a) Schematic illustrations of the discharge process and (b) free-energy profiles for the S_8 and Li_2S_n (n = 1, 2, 4, 6, 8) conversion under the catalytic effects of VC nanosheet.

Table S1. Comparing adsorption energies (in eV) of Li_2S, Li_2S_4, Li_2S_6, and Li_2S_8 for different anchoring materials with typically used organic electrolytes.

Substrate	Li_2S	Li_2S_4	Li_2S_6	Li_2S_8	Ref
DME	–	0.80	≈ 0.85	0.78	[1]
DOL	–	0.80	≈ 0.83	0.77	[1]
VC	4.25	3.19	2.28	2.09	This work
CrC	≈ 4.00	3.16	1.59	1.89	This work
FeC	3.98	2.61	1.88	0.81	This work
Graphene	0.62	0.60	0.78	0.70	[1]
C_3B	1.82	≈ 1.15	≈ 1.10	≈ 0.90	[1]
C_3N	0.74	0.73	0.99	1.11	[1]
C_5N	≈ 1.60	≈ 1.10	≈ 1.12	≈ 1.25	[2]
BGDY	–	1.00	0.90	0.85	[2]
$NDGY-C_{36}N_6$	–	1.52	1.25	1.22	[2]
BC_2N	1.37	0.72	0.77	1.06	[3]
Defective borophene	–	2.67	2.53	2.87	[4]
Phosphorene	2.51	1.27	1.00	1.12	[5]
Boron-phosphide	2.85	1.63	0.87	0.95	[6]
TiS_2	–	≈ 1.40	≈ 0.90	≈ 1.20	[7]
MoS_2	–	≈ 0.90	≈ 0.80	≈ 0.75	[7]

| VS$_2$ | 4.44 | 2.42 | 1.14 | 1.69 | [8] |

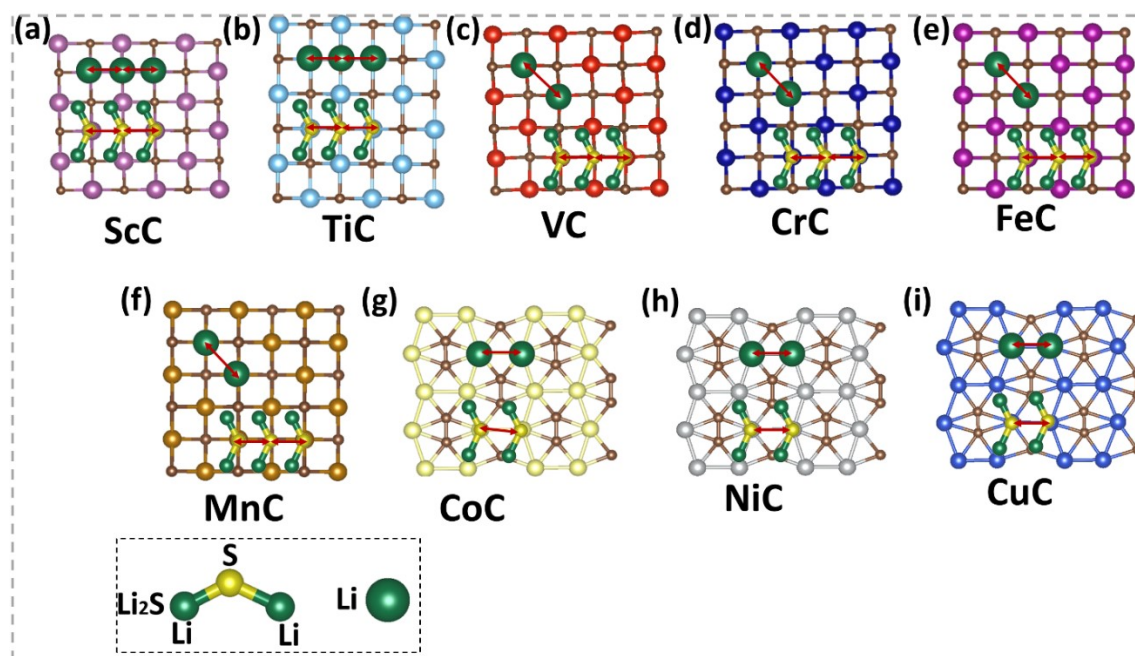'–' indicates that no data is available.

Figure S16. Migration pathways for Li-ion and short-chain Li$_2$S molecule on the (a) ScC, (b) TiC, (c) VC, (d) CrC, (e) MnC, (f) FeC, (g) CoC, (h) NiC, and (i) CuC.
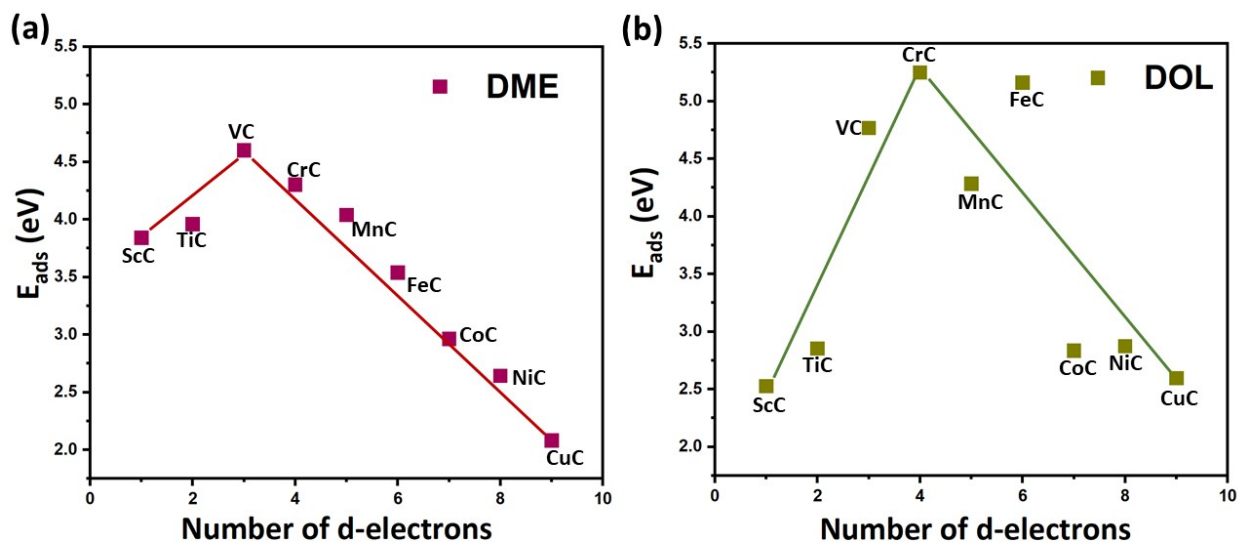

Figure S17. The total adsorption energies of Li$_2$S molecule with ScC, TiC, Vc, CrC, MnC, FeC, CoC, NiC, and CuC substrates with (a) DME and (b) DOL electrolytes interface.
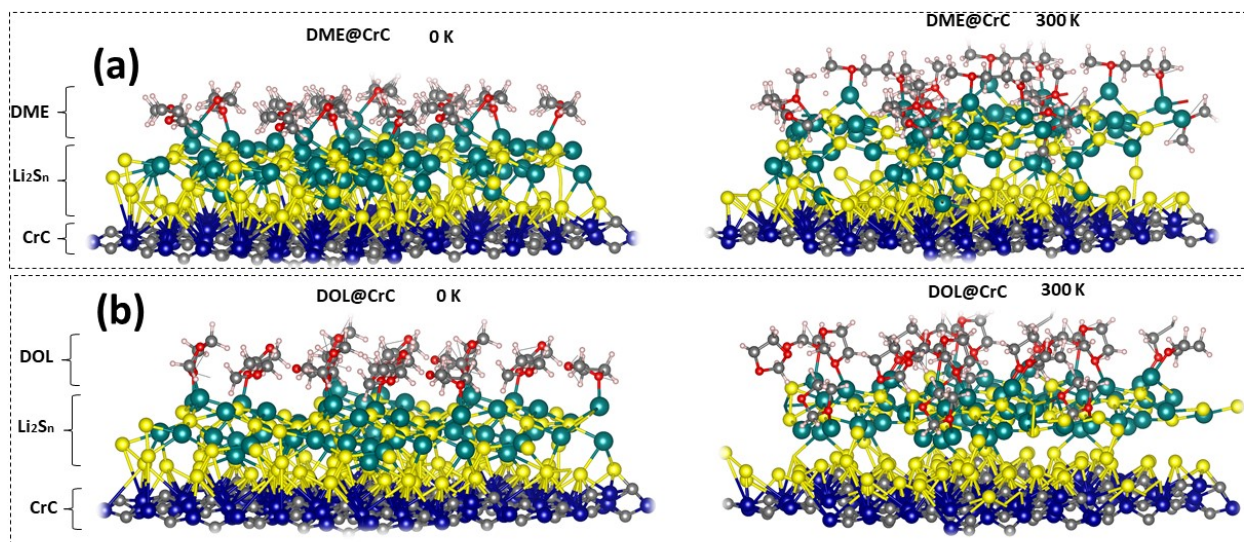
Figure S18. Geometric illustration of $8S_8+nLi+8DME/DOL$ anchored on supercell of CrC-based model at 0 K and 300 K during AIMD calculations for 10 psec.
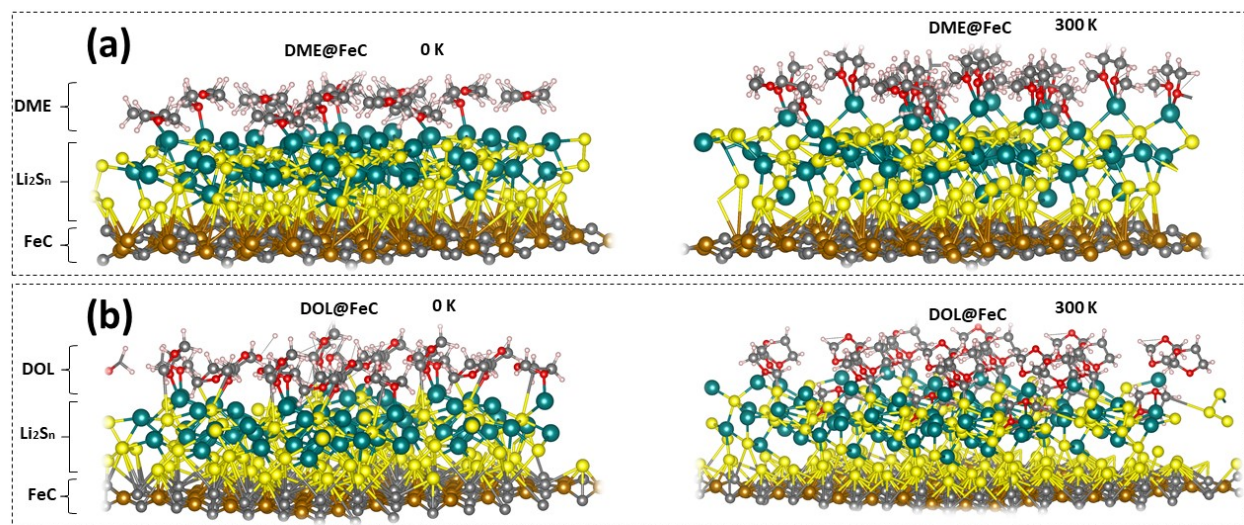

Figure S19. Geometric illustration of $8S_8+nLi+8DME/DOL$ anchored on supercell of FeC-based model at 0 K and 300 K during AIMD calculations for 10 psec.
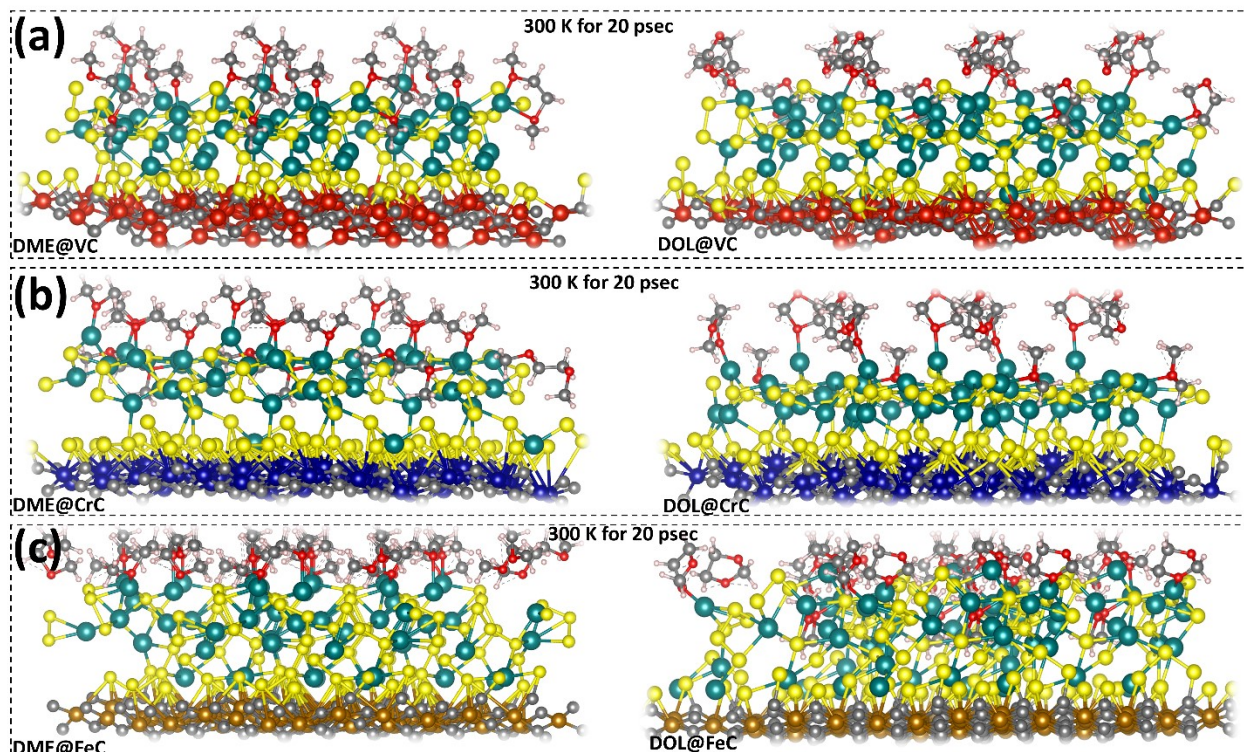
Figure S20. Geometric illustration of $8S_8+nLi+8DME/DOL$ anchored on supercell of (a) VC, (b) CrC, and (c) FeC-based model at 300 K during AIMD calculations for 20 psec.
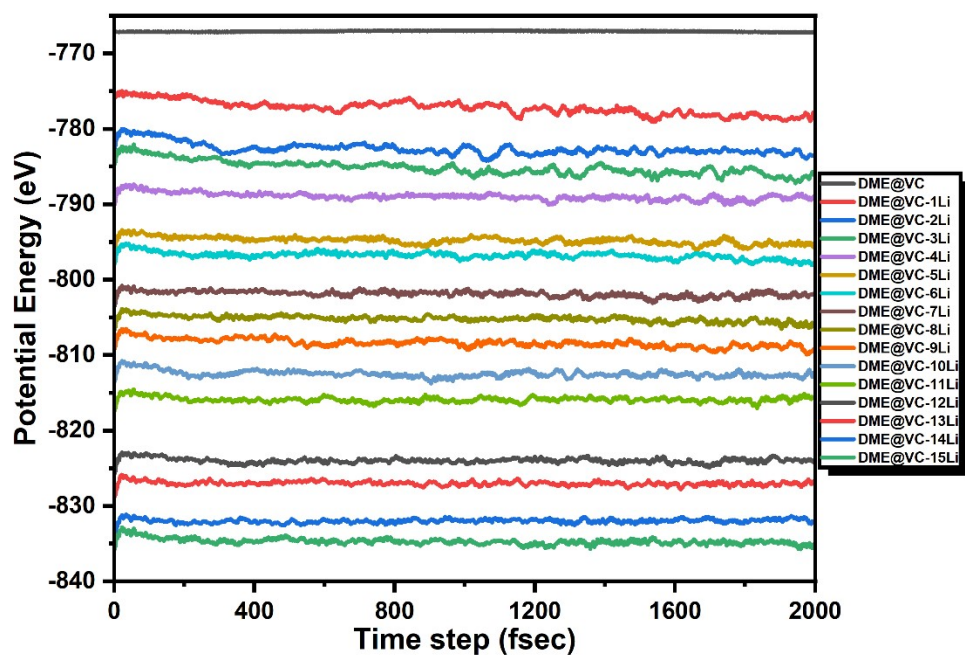

Figure S21. The fluctuations in potential energy for increasing concentration of Li-ion in $8S_8+nLi+8DME$ anchored on supercell of VC nanosheet during AIMD calculations for 2 psec at a temperature of 300 K. ($0 < n < 15$)

Figure S22. The fluctuations in potential energy for increasing concentration of Li-ion in $8S_8+nLi+8DOL$ anchored on supercell of VC nanosheet during AIMD calculations for 2 psec at a temperature of 300 K. (Where $0 < n < 15$).

Figure S23. The fluctuations in potential energy for increasing concentration of Li-ion in $8S_8+nLi+8DME$ anchored on supercell of CrC nanosheet during AIMD calculations for 2 psec at a temperature of 300 K. ($0 < n < 15$)
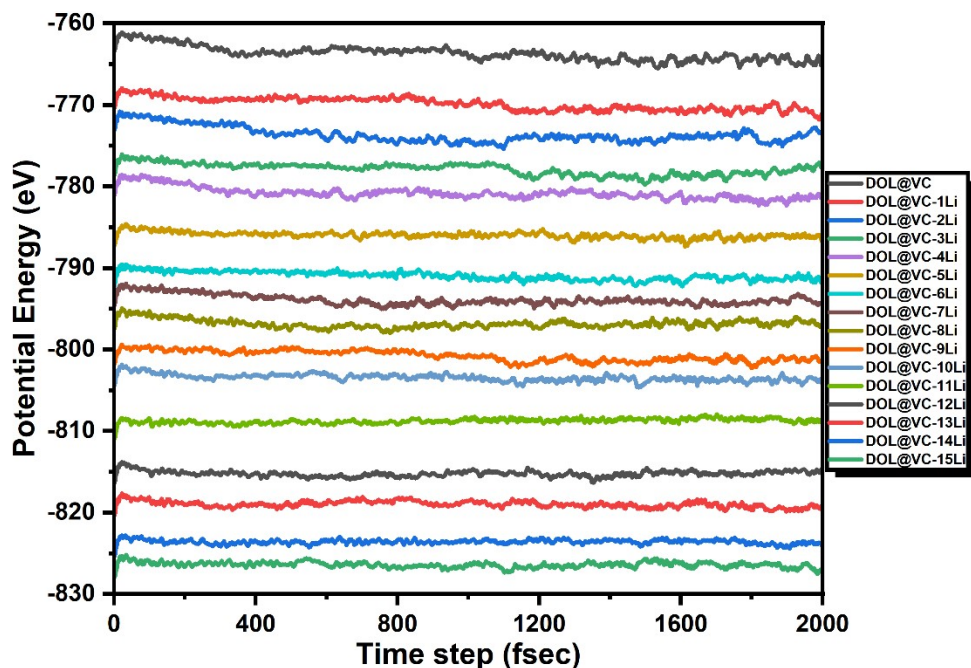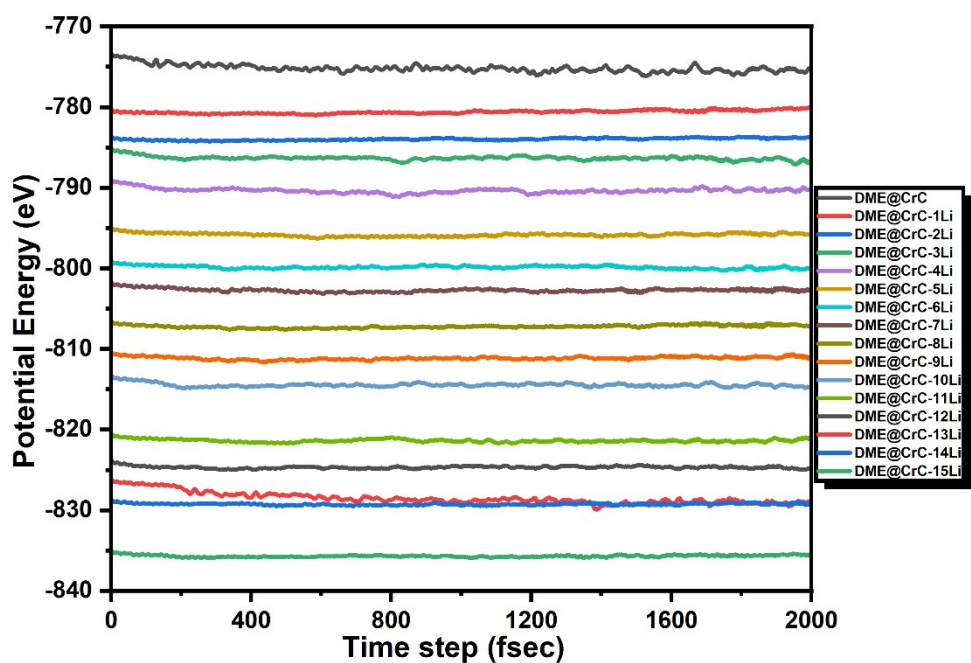
Figure S24. The fluctuations in potential energy for increasing concentration of Li-ion in $8S_8+nLi+8DOL$ anchored on supercell of CrC nanosheet during AIMD calculations for 2 psec at a temperature of 300 K. ($0 < n < 15$).

Figure S25. The fluctuations in potential energy for increasing concentration of Li-ion in $8S_8+nLi+8DME$ anchored on supercell of FeC nanosheet during AIMD calculations for 2 psec at a temperature of 300 K. ($0 < n < 15$).
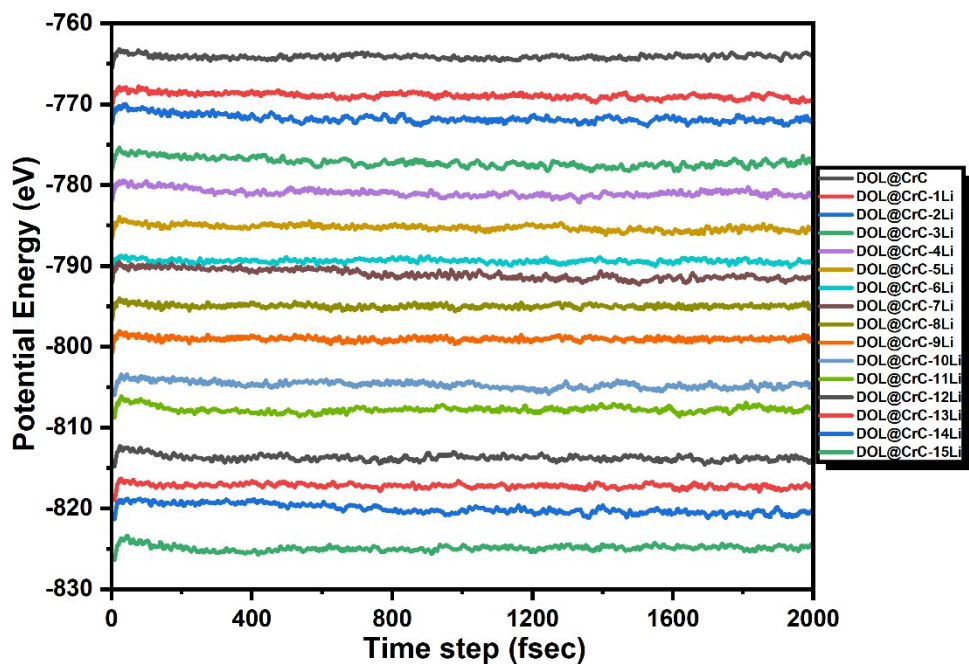
Figure S26. The fluctuations in potential energy for increasing concentration of Li-ion in $8S_8+nLi+8DOL$ anchored on supercell of FeC nanosheet during AIMD calculations for 2 psec at a temperature of 300 K. (0 < n < 15)
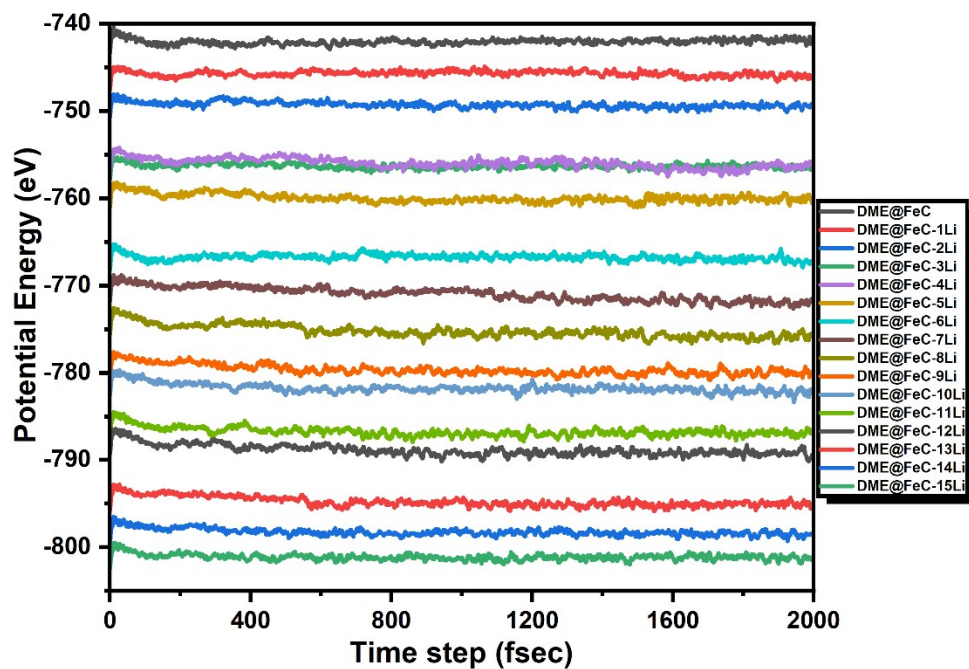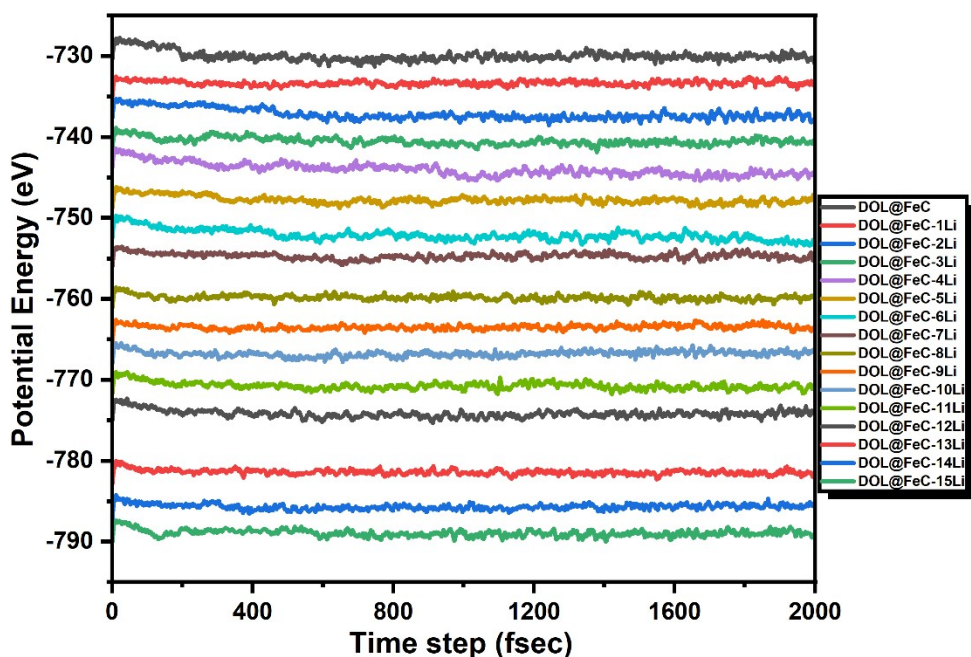
References

1 Y. Qie, J. Liu, S. Wang, S. Gong and Q. Sun, *Carbon*, 2018, **129**, 38–44.

2 I. Muhammad, U. Younis, H. Xie, Y. Kawazoe and Q. Sun, *Adv. Theory and Simulations*, 2020, **3**, 1–7.

3 Y. Shao, Q. Wang, L. Hu, H. Pan and X. Shi, *Carbon*, 2019, **149**, 530–537.

4 H. R. Jiang, W. Shyy, M. Liu, Y. X. Ren and T. S. Zhao, *J. Mater. Chem. A*, 2018, **6**, 2107–2114.

5 Y. Wang, Q. Zhang, M. Jia, D. Yang, J. Wang, M. Li, J. Zhang, Q. Sun and Y. Jia, *Appl. Surf. Sci.*, 2016, **363**, 318–322.

6 T. T. Yu, P. F. Gao, Y. Zhang and S. L. Zhang, *Appl. Surf. Sci.*, 2019, **486**, 281–286.

7 Q. Zhang, Y. Wang, Z. W. Seh, Z. Fu, R. Zhang and Y. Cui, *Nano Lett.*, 2015, **15**, 3780–3786.

8 Y. Wang, F. Wang, Z. Ma, N. Song, T. Zhang, Q. Zhang and D. Yang, *Chem. Phys. Lett.*, 2020, **741**, 137121.